

Nanoparticles | Hot Paper |

Structure Evolution and Associated Catalytic Properties of Pt–Sn Bimetallic Nanoparticles

Hongpan Rong,^[a] Zhiqiang Niu,^{*[a]} Yafan Zhao,^[a] Hao Cheng,^[b] Zhi Li,^[a] Lei Ma,^[a] Jun Li,^[a] Shiqiang Wei,^[b] and Yadong Li^{*[a]}

Abstract: Bimetallic nanoparticles (NPs) often show new catalytic properties that are different from those of the parent metals. Carefully exploring the structures of bimetallic NPs is a prerequisite for understanding the structure-associated properties. Herein, binary Pt–Sn NPs with tunable composition are prepared in a controllable manner. X-ray characterizations reveal that their structures evolve from SnO_{2-x}-patched PtSn alloys to SnO_{2-x}-patched Pt clusters when more tin

is incorporated. An obvious composition-dependent catalytic performance is observed for the hydrogenation of α,β -unsaturated aldehydes: the selectivity to unsaturated alcohol increases substantially at high tin content, whereas the reaction rate follows a volcano shape. Furthermore, Pt sites are responsible for hydrogen dissociation, whereas oxygen vacancy (O_{vac}) sites, provided by SnO_{2-x}, drastically enhance the adsorption of carbonyl group.

Introduction

Bimetallic NPs represent an important class of heterogeneous catalysts in hydrocarbon reforming.^[1] Meanwhile, their applications in biomass refinery and electro-catalysis are growing rapidly.^[2] This is related to the unusual properties of bimetallic catalysts that originate from the synergistic effects between the two parent metals.^[3] However, the complexity of the bimetallic nanoparticles (e.g., crystal facets,^[4] size,^[5] chemical states, and the interface of different domains^[6]) makes it difficult to unambiguously determine the function of each constituent metal in the catalytic process.^[7] Understanding catalytic enhancement requires at least independent control over the composition of the bimetallic catalysts while maintaining their other structural parameters, such as size and morphology. Meanwhile, it should be noted that the composition variation might induce restructuring of the bimetallic nanoparticles. In the Pt_xCo NPs, for example, Co is distributed in a concentration gradient and gradually depletes from the core to Pt-rich surface region when $x \leq 3$, whereas Co is evenly distributed within the NP when $x \geq 4$.^[8]

Selective hydrogenation of α,β -unsaturated aldehydes to unsaturated alcohols (UAs) is a fundamental catalytic process for the production of fine chemicals^[9] as well as an essential step

in the catalytic conversion of biomass.^[10] Although thermodynamics favors the formation of saturated aldehydes over that of UAs,^[11] the latter can be selectively produced on modified bimetallic Pt-based catalysts by tailoring their facet, size, support material, and composition. For instance, hydrogenation of prenal on Pt(111) produced UA with a selectivity of 65%, whereas for the reaction on Pt(110) only saturated products were observed.^[12] In the hydrogenation of crotonaldehyde, the selectivity to UA increased with increasing particle size of Pt catalysts.^[13] The selectivity in the hydrogenation of α,β -unsaturated aldehydes is affected by the support materials as well. Whereas SiO₂ and Al₂O₃ exhibited no promoting effect, TiO₂-supported catalyst with Ti³⁺ or oxygen vacancies showed an enhanced selectivity to UA.^[14] The electron transfer can be achieved by incorporating an electropositive metal (e.g., Fe, Co, Ni, Ge, and Sn) into the catalytically active Pt.^[15] Meanwhile, the electron-deficient metal atoms acted as Lewis acid adsorption sites for C=O.^[16] All of above-mentioned observations demonstrate that the selectivity of Pt-based bimetallic nanocatalysts is governed by a complex set of factors. Differentiating the role of each factor relies greatly on the monodispersity of the catalyst.

Herein, we try to contribute to a better understanding on the role of Pt-based bimetallic catalysts in the selective hydrogenation of α,β -unsaturated aldehydes. To this end, we synthesized monodisperse Pt–Sn nanoparticles with a tunable composition. X-ray absorption fine structure (XAFS) studies indicated that the structure of Pt–Sn nanoparticles evolved from the SnO_{2-x}-patched PtSn alloy to the SnO_{2-x}-patched Pt cluster as the atomic ratio of Sn/Pt increased, and the amount of surface SnO_{2-x} was directly proportional to the Sn/Pt ratio. We used cinnamaldehyde (CAL) as the model substrate of α,β -unsaturated aldehydes. Selective hydrogenation of CAL was then performed at ambient condition; the reaction showed that both

[a] H. Rong, Dr. Z. Niu, Dr. Y. Zhao, Z. Li, Dr. L. Ma, Prof. J. Li, Prof. Y. Li
Department of Chemistry and
Collaborative Innovation Center for Nanomaterial Science and Engineering
Tsinghua University, Beijing 100084 (P.R. China)
E-mail: ydli@mail.tsinghua.edu.cn
zqniu@mail.tsinghua.edu.cn

[b] H. Cheng, Prof. S. Wei
National Synchrotron Radiation Laboratory and
University of Science & Technology of China
Hefei, Anhui 230029 (P.R. China)

Supporting information for this article is available on the WWW under
<http://dx.doi.org/10.1002/chem.201501442>.

the selectivity and activity were dependent on the coverage density of surface SnO_{2-x} . The selectivity to cinnamyl alcohol (COL) reached up to 92% at a high coverage density of SnO_{2-x} . X-ray photoelectron spectroscopy (XPS) analysis revealed that low-valent Sn^{2+} predominated at high SnO_{2-x} coverage, meaning more oxygen vacancy sites were available for CAL adsorption. Density functional theory (DFT) calculations indicated that the preferential adsorption of the C=C bond was not affected when oxygen vacancy sites were introduced to the catalysts.

Results and Discussion

Characterization of Pt–Sn catalysts

Transmission electron microscopy (TEM) images showed that the as-prepared Pt (Figure 1a) and Pt–Sn NPs (Figure 1b and

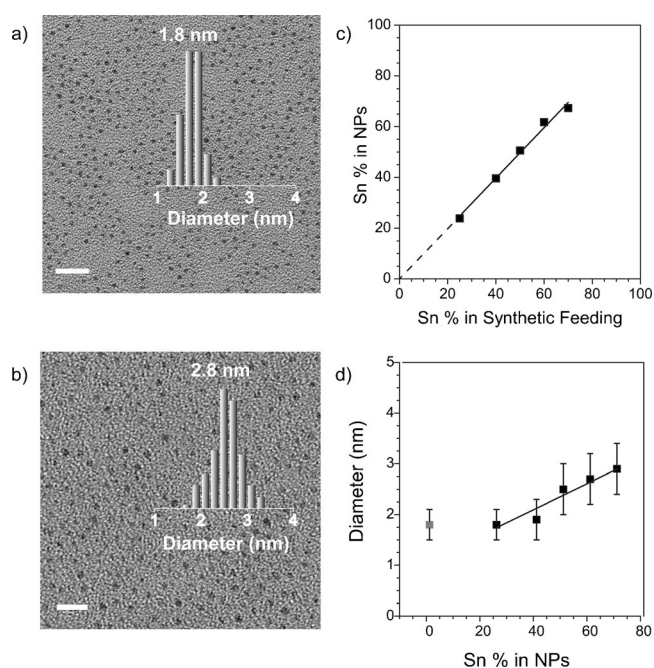


Figure 1. TEM images of as-prepared a) Pt- and b) Pt₅₀Sn₅₀ NPs; c) Plot of Sn % in Pt–Sn NPs as a function of Sn% in synthetic feeding (slope = 1.0; $R^2 = 0.99$); d) Plot of the diameter of Pt–Sn NPs as a function of Sn % in NPs.

the Supporting Information, Figure S1) were all uniform spherical particles with narrow size distributions. The lattice distance in the high-resolution (HR)TEM image of Pt₅₀Sn₅₀ was 0.23 nm, close to the value (0.227 nm) of fcc Pt(111) (the Supporting Information, Figure S2a). The distributions of Pt and Sn were clearly resolved by energy-dispersive X-ray spectroscopy (EDX) elemental mapping (the Supporting Information, Figure S2c, d), which suggested an even distribution of the Pt and Sn throughout the entire Pt₅₀Sn₅₀ NPs. The composition of the Pt–Sn NPs were tuned by varying the feeding ratio of $[\text{SnCl}_2] \cdot 2\text{H}_2\text{O}/[\text{Pt}(\text{acac})_2]$ (acac = acetylacetonate) and analyzed by EDX (the Supporting Information, Table S1). There is a linear correlation (slope = 1.0) between the synthetic feeding ratio of Sn and atomic percentage (Sn%) in the final bimetallic NPs

(Figure 1c). Meanwhile, the particle size slightly increased along with the Sn content, but the size was confined to a narrow range of 1.8–2.9 nm (Figure 1d). These results demonstrate that our synthetic method affords efficient composition control over Pt–Sn NPs at a confined size range, which provided a suitable system to investigate the composition dependence of Pt–Sn NPs in the catalyst.

X-ray absorption fine structure (XAFS) studies were performed on freshly prepared Pt–Sn NPs to study the electronic modification and the local atomic arrangement of Pt and Sn. Figure 2a shows the normalized X-ray absorption near-edge structure (XANES) spectra at the Pt–L_{III}-edge. A substantial decrease of the white line intensity was observed for Pt–Sn NPs as compared with Pt NPs and PtO₂. The intensity of the white line is an indicator of the d-state occupancy.^[17] Both the decrease of the white line at the Pt–L_{III}-edge as compared with Pt NPs and the increase of the white line at the Sn–k-edge as compared with Sn foil (Figure 2b) of Pt–Sn NPs, therefore, could be attributed to the electron transfer from surrounding Sn to Pt.

Figure 2c shows Fourier transforms (FTs) of k^2 -weighted extended X-ray absorption fine structure (EXAFS) oscillations at the Pt–L_{III}-edge. The main peaks of FTs for Pt and Pt–Sn NPs located in the range of 2–3 Å were assigned to either Pt–Pt or Pt–Sn bonds, and there were very weak peaks at about 1.6 Å from the Pt–O bonds. Quantitative curve fittings of XAFS data were performed, and the results are summarized in Table S2 (the Supporting Information). As compared with Pt NPs (8.0), the Pt–Pt coordination number in Pt₇₅Sn₂₅, Pt₆₀Sn₄₀, and Pt₅₀Sn₅₀ NPs was only about five. This suggested the formation of PtSn alloy, in which Sn atoms diluted the Pt atoms. However, Pt–Sn contributions were not observed for Pt₄₀Sn₆₀ and Pt₃₀Sn₇₀ NPs, indicating the phase segregation of Sn and Pt. Figure 2d shows the FTs of k^2 -weighted EXAFS oscillations at the Sn–K-edge for Pt–Sn NPs and reference Sn foil. The main peaks of FTs for Pt–Sn NPs were all located in the region of 1–2 Å and assigned to Sn–O contributions, whereas the weak peaks at 2–3 Å were assigned to Sn–Pt and Sn–Sn contributions. The EXAFS data of Pt–Sn NPs suggested a detailed picture of their structural evolution with the variation of composition (Figure 3). At low Sn content, the structure of Pt₇₅Sn₂₅, Pt₆₀Sn₄₀, and Pt₅₀Sn₅₀ NPs was a PtSn alloy patched by tin oxides, whereas at high Sn content, the structure of Pt₄₀Sn₆₀ and Pt₃₀Sn₇₀ NPs was a Pt cluster patched by tin oxides.

The proposed structural evolution depicted in Figure 3 was further verified by X-ray diffraction (XRD) studies. As shown in Figure S3 (the Supporting Information), only a broad peak assigned to the (111) diffraction of fcc Pt was observed for Pt NPs. The peak positions of (111) diffraction for Pt₇₅Sn₂₅, Pt₆₀Sn₄₀, and Pt₅₀Sn₅₀ continuously shifted to slightly lower 2θ values compared with those of Pt NPs, suggesting the formation of PtSn alloy. However, the peak positions of (111) diffraction for Pt₄₀Sn₆₀ and Pt₃₀Sn₇₀ regained similar values as compared to Pt NPs. This observation indicated that the Sn atoms no longer replaced the Pt atoms to form a bimetallic phase. Instead, the Pt atoms formed Pt clusters in a pure phase. In addition, a small peak showed up at the 2θ value of $\approx 30^\circ$ for Pt₄₀Sn₆₀

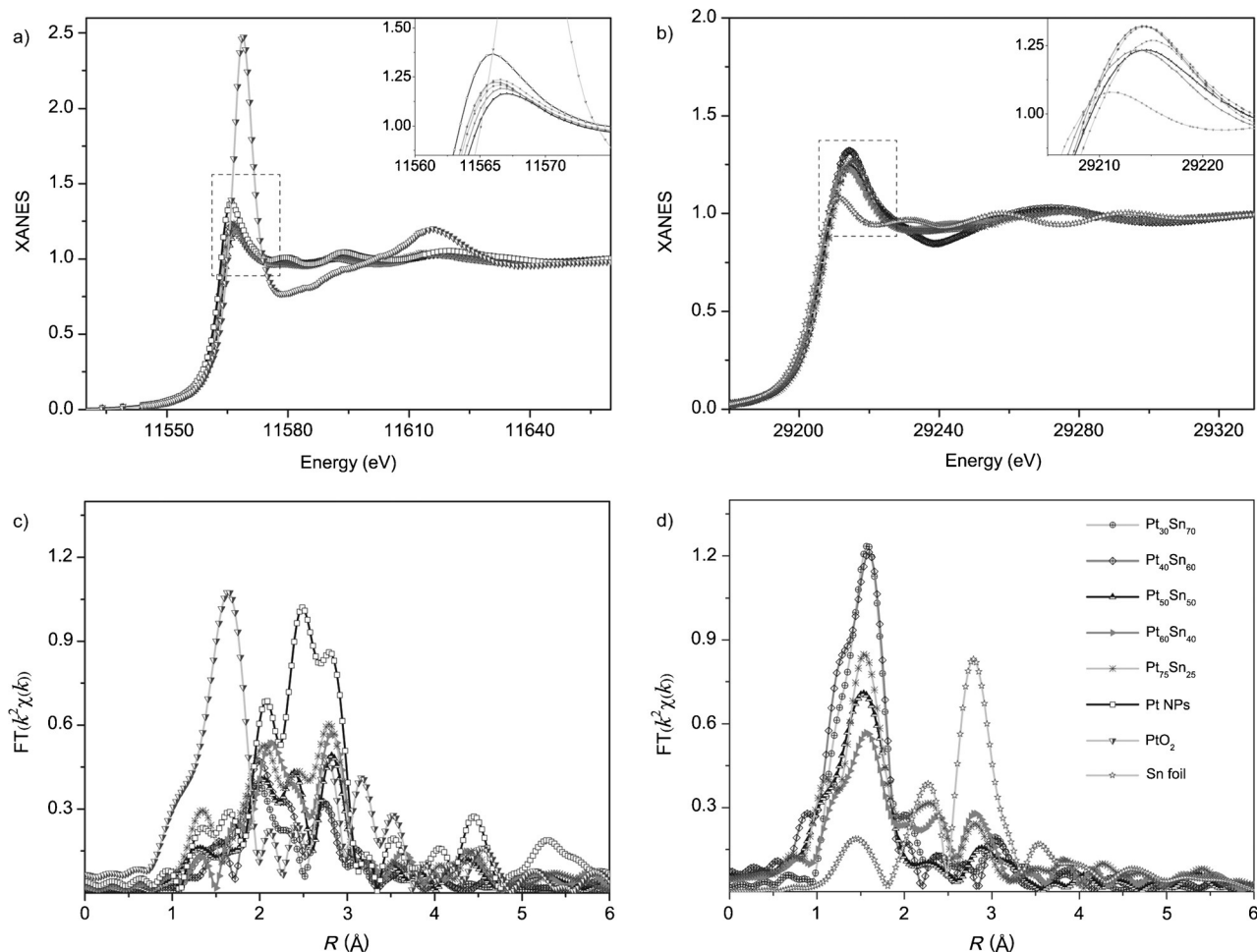


Figure 2. a) Normalized Pt-L_{III}-edge and b) Sn-K-edge XANES spectra of freshly-prepared Pt–Sn NPs. Fourier transforms (FTs) of c) Pt-L_{III}-edge k^3 -weighted and d) Sn-K-edge k^2 -weighted EXAFS oscillations $\chi(k)$ of freshly-prepared Pt–Sn NPs as compared with Pt NPs, PtO₂, and Sn foil. Insets show the enlarged pictures of the corresponding square sections.

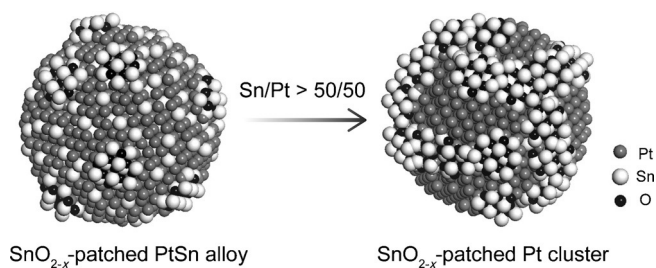


Figure 3. Scheme of the structural evolution of the Pt–Sn bimetallic clusters with an increase of the tin content: SnO_{2-x}-patched PtSn alloy (left) at low Sn content when the atomic ratio of Sn/Pt \leq 50:50, otherwise they become SnO_{2-x}-patched Pt cluster (right).

and Pt₃₀Sn₇₀, which could be assigned to the diffraction of SnO(101). This is because the crystalline grain of surface tin oxides grew larger as the Sn content increased.

X-ray photoelectron spectroscopy (XPS) measurements were performed to investigate the chemistry at the surface of Pt–Sn NPs; the results are listed in Table S3 (the Supporting Information). Figure 4 shows the Sn 3d_{5/2} and Pt 4f doublet XPS spec-

tra of as-prepared Pt and Pt–Sn NPs. The Pt 4f_{7/2} peak for Pt NPs and Pt–Sn NPs could be deconvoluted into two doublets assigned to Pt⁰ (71.4 eV) and Pt²⁺ (72.4 eV) species. For Pt–Sn NPs, the addition of Sn into Pt greatly enhances the percentages of reduced Pt⁰ as compared with Pt NPs. The ratio of Pt⁰/Pt²⁺ was 0.59 for Pt NPs, whereas the values for Pt–Sn NPs were all around 2 (Figure 4b). As marked by the dark gray area in Figure 4c, the Pt⁰ core-level continuously shifted to higher binding energy along with the increased Sn content in bimetallic Pt₇₅Sn₂₅ (71.4 eV), Pt₆₀Sn₄₀ (71.5 eV), and Pt₅₀Sn₅₀ (71.7 eV). The positive core-level shift of Pt⁰ was consistent with the electron exchange between Pt and Sn in the alloy phase.^[18] After a further increase in the Sn content to Pt₄₀Sn₆₀ and Pt₃₀Sn₇₀, the Pt⁰ core-level reversely shifted to lower binding energy (light gray area in Figure 4c), which indicated that the electron exchange between Pt and Sn gradually became weak (as demonstrated by XAFS and XRD studies) because of the phase segregation.

The Sn 3d_{5/2} peaks could be deconvoluted into features assigned to Sn⁰, Sn²⁺, and Sn⁴⁺ oxide species. The ratio of Sn²⁺/Sn⁴⁺ drastically increased from 0.4 to 3.5 as the Sn percentage in the Pt–Sn NPs increased (Figure 4b). The binding energy

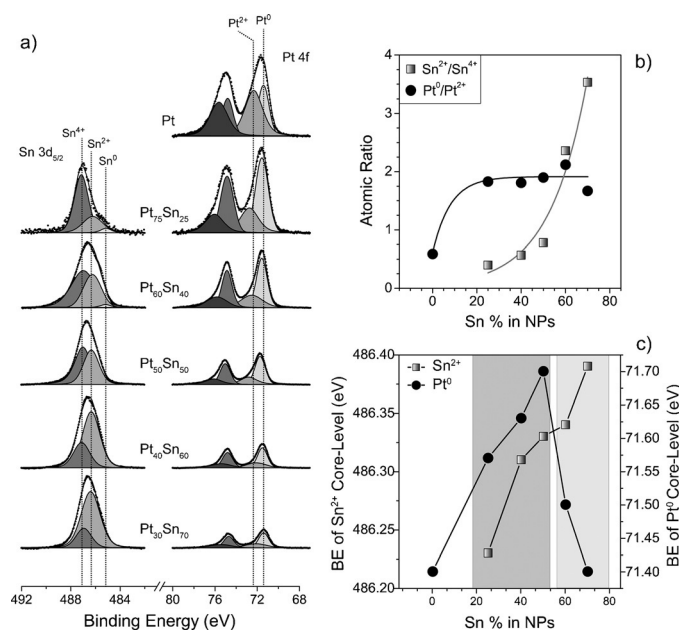


Figure 4. a) Sn 3d_{5/2} and Pt 4f XPS spectra for Pt and Pt–Sn NPs with varied composition; b) Plot of atomic ratios of Pt⁰/Pt²⁺ and Sn²⁺/Sn⁴⁺, which were determined by the peak area ratio from XPS spectra; c) Sn²⁺ and Pt⁰ core-levels as a function of Sn % in the as-prepared NPs. The dark gray area in c) denotes the SnO_{2-x}-patched PtSn alloy, whereas the light gray area denotes SnO_{2-x}-patched Pt cluster.

values for the Sn²⁺ core-level shifted positively with an increase in the percentage of Sn in the Pt–Sn NPs (Figure 4c).

In situ FTIR spectroscopy of adsorbed CO on the catalysts was performed to obtain further surface information. As shown in Figure S4 (the Supporting Information), the high frequency IR bands $\approx 2050\text{ cm}^{-1}$ were due to linearly adsorbed CO, whereas the low frequency bands at 1830 cm^{-1} were due to bridge-bonded CO species.^[19] The adsorbed CO continuously decreased as the Sn content increased, indicating a sustained decrease of the exposed Pt sites. Moreover, few bridge-bonded CO species were observed when the Sn content was above 40%, which implies the division of adjacent Pt atoms by Sn atoms. It should be noted that the amount of surface tin oxides was directly proportional to the amount of Pt. Therefore, the coverage density of tin oxides on the particle surface should increase with a decrease in Pt sites.

Selective hydrogenation of cinnamaldehyde on Pt–Sn

We next examined the selective hydrogenation of α,β -unsaturated aldehydes by using cinnamaldehyde (CAL) as a model substrate. Figure S5 (the Supporting Information) shows the reaction pathway for the hydrogenation of CAL, which in parallel produces hydrocinnamaldehyde (HCAL) and desired cinnamyl alcohol (COL) through the reduction of a carbon–carbon double bond or carbonyl group. Consecutive reduction of HCAL or COL leads to hydrocinnamyl alcohol (HCOL).

The product distributions for CAL hydrogenation along with the reaction time were investigated for monometallic Pt and

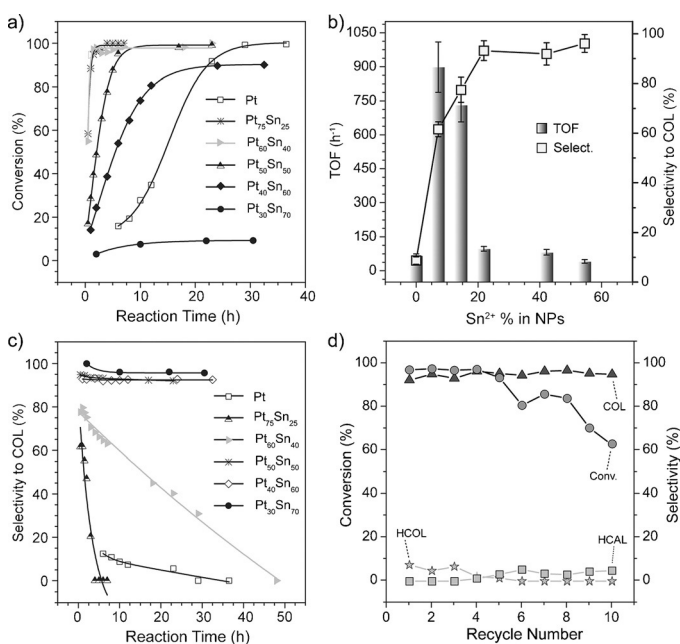


Figure 5. a) Conversion of CAL with Pt and Pt–Sn catalysts as a function of reaction time; b) Influence of the SnO coverage density on the TOF and COL selectivity for the CAL hydrogenation. The SnO content was estimated from XPS analysis. Cyclic voltammetry (CV) was used to determine the exposed Pt atoms; these were then used as active sites to calculate the TOF value (the Supporting Information, Figure S8); c) Selectivity to COL with Pt and Pt–Sn catalysts as a function of reaction time; d) The catalytic performance of Pt₅₀Sn₅₀ in the recycling study.

for different Pt–Sn NPs (the Supporting Information, Figure S6); the conversion rate of CAL is plotted in Figure 5a. With monometallic Pt NPs as the catalyst, only 16% of CAL was converted to products in 6 h. However, a significant acceleration of the reaction rate was observed with the addition of Sn to Pt (Pt₇₅Sn₂₅). The turnover frequency (TOF) of Pt₇₅Sn₂₅ was more than tenfold higher than that of pure Pt NPs when the conversion of CAL was $\approx 20\%$ (the conversion of Pt₃₀Sn₇₀ was 7.5% as an exception, Figure 5b). However, when Pt was completely covered by tin oxide species (the Supporting Information, Figure S7), the hydrogenation of CAL did not occur. This observation indicates that the Pt sites are necessary for producing hydrogen atoms. In previous report, the enhanced conversion rate of Pt–Sn bimetallic catalysts was attributed to the creation of a new kind of active site by adding Sn to Pt.^[20] On the other hand, our study has demonstrated that the addition of Sn significantly improved the Pt⁰/Pt²⁺ ratio. As estimated from the XPS analysis, the percentages of reduced Pt⁰ species in the NPs were 37.1, 48.5, 38.8, 32.8, 27.2, and 18.8% for Pt, Pt₇₅Sn₂₅, Pt₆₀Sn₄₀, Pt₅₀Sn₅₀, Pt₄₀Sn₆₀, and Pt₃₀Sn₇₀, respectively. Accordingly, Pt₇₅Sn₂₅ and Pt₆₀Sn₄₀ might have more reduced-Pt⁰ sites on the surface than monometallic Pt for H₂ dissociation. Further enhancing the tin percentage in the bimetallic NPs continuously reduced the conversion rate of CAL, which could be due to the decreased surface Pt⁰ sites because of increased coverage of Pt by the tin species. Therefore, the synergy between the Pt sites and SnO sites leads to an optimum Sn/Pt ratio.

With monometallic Pt as the catalyst, the hydrogenation preferentially occurred on the C=C bond and the selectivity to desired COL was < 12% throughout the reaction (Figure 5c). HCAL was preferentially produced as the primary intermediate and further hydrogenated to HCOL (the Supporting Information, Figure S6). The addition of Sn exerted a great influence on the reaction pathway. As shown in Figure 5b, the selectivity to COL, which was measured at about 60% conversion of CAL (the conversion of Pt₃₀Sn₇₀ was 7.5% as an exception), increased from 6 (Pt) to 62 (Pt₇₅Sn₂₅), 77 (Pt₆₀Sn₄₀), and > 90 (Pt₅₀Sn₅₀, Pt₄₀Sn₆₀, and Pt₃₀Sn₇₀), respectively. The product distributions (the Supporting Information, Figure S6) demonstrated that the reaction proceeded through preferential hydrogenation of C=O bond for bimetallic Pt–Sn NPs. The selectivity delivered by Pt₇₅Sn₂₅ and Pt₆₀Sn₄₀ NPs declined rapidly, leaving HCOL as the final product. In contrast, Pt₅₀Sn₅₀, Pt₄₀Sn₆₀, and Pt₃₀Sn₇₀ NPs maintained their selectivity at the initial level (above 90%) with prolonged reaction time.

The efficiency of a reaction system is determined by a combination of conversion and selectivity. A higher conversion means minimum recycling of the reactant, and a higher selectivity means fewer purification steps. In this case, Pt₅₀Sn₅₀ is the most efficient catalyst among all those investigated. It achieved > 99% conversion of CAL and 92% selectivity to COL at ambient conditions. With this highly efficient catalyst in hand, we then set out to investigate its stability. As shown in Figure 5d, both the conversion of CAL and the selectivity to COL remained stable in the first five cycles of reuse. Starting from the sixth cycle, the conversion of CAL gradually decreased, whereas the selectivity to COL was maintained above 90%. An EDX study indicated that the composition of Pt₅₀Sn₅₀ NPs after ten cycles of reuse remained almost the same as those of the fresh ones (the Supporting Information, Figure S11). The decreased catalytic activity could be attributed to the mass loss during catalyst recovery, and aggregation of the used catalyst (the Supporting Information, Figure S12) could also lead to the decline of the active surface.

It should be noted that separated Pt and tin oxides (the Supporting Information, Figure S9) with the same composition as Pt₅₀Sn₅₀ NPs exhibited an increased CAL conversion rate but a decreased COL selectivity (the Supporting Information, Figure S10). This control experiment suggested that the close contact of Pt sites with tin oxides might be a requirement for the production of desired COL. A similar result was observed in a previous study.^[21]

DFT calculations and the reaction mechanism

For the selective hydrogenation of α,β -unsaturated aldehyde, the adsorption of CAL on the catalyst is the first step. By comparing the calculated adsorption energies of C=O and C=C bond through density functional theory, we could make an estimation about the activation priority of these two kinds of double bonds.^[22]

First, we investigated the adsorption of CAL on Pt (111) surface as a benchmark for our calculation. The most stable configuration for CAL adsorption on Pt (111) surface is a η^4 -di- σ (C=

O)-di- σ (C=C) structure (the Supporting Information, Figure S13a) with an adsorption energy of –1.14 eV. For the adsorption of C=C bond on the Pt (111) surface, both the η^2 -di- σ (C=C) configuration (the Supporting Information, Figure S13b) and the η^2 - π (C=C) configuration (Figure S13c) were investigated, and the adsorption energies were –0.90 and –0.60 eV, respectively. The atop adsorption for C=O (the Supporting Information, Figure S13d) is much weaker, having an adsorption energy of –0.55 eV. All these adsorption energies (Table 1) are in good agreement with the calculated values reported by Yang et al.^[22] From these adsorption energies, we can see that the C=C bond activation is in preference to the C=O bond activation on the Pt(111). This is in consistent with our observation that the hydrogenation preferentially occurred on the C=C bond on monometallic Pt.

Table 1. Calculated adsorption of CAL on different surfaces: Pt (111), Pt₆/SnO_{2-x} (110), and Pt₆/SnO_{2-x} (110) with one O_{vac}.

Surface	E_{ads} [eV] ^[a]			
	Pt(111)	Pt(111) ^[22]	Pt ₆ /SnO _{2-x} (110)	Pt ₆ /SnO _{2-x} (110) with one O _{vac}
η^4 -di- σ (C=O)-di- σ (C=C)	–1.14	–1.11	N/A	N/A
atop adsorption on Pt	–0.90	–1.07	–0.67	–0.93
η^2 -di- σ (C=C)	–0.60	–0.58	–1.01	–1.10
η^2 - π (C=C)	–0.55	–0.46	–1.02	–1.05
atop adsorption on Sn	N/A	N/A	–0.51	–1.13

[a] N/A = No adsorption.

We then built a catalyst model, namely, the Pt₆/SnO_{2-x} (110) surface, according to the coordination number of the EXAFS data of Pt₅₀Sn₅₀ alloy, to investigate the adsorption of CAL. Experimentally, the fitted coordination numbers for Pt–Sn and Pt–Pt in Pt₅₀Sn₅₀ alloy are 1.7 and 5.2, respectively (the Supporting Information, Table S2). As shown in Figure S14a and b (the Supporting Information), the model was constructed by placing six Pt atoms on the SnO₂ surface, taking the place of 5 O atoms and 1 Sn atom. In this catalyst model, the average coordination number of Pt–Sn is 1.6, in reasonable agreement with the experimental value. The coordination number of the Pt atom in the center of all six Pt atoms is 5. The adsorption of CAL on this catalytic model was then investigated. For the adsorption of C=O bond on Pt atom, the most stable atop adsorption configuration (the Supporting Information, Figure S14c) has an adsorption energy of –0.67 eV. It is also possible that the C=O bond is adsorbed onto the Sn atoms. For the η^2 -di- σ (C=C) adsorption on Pt atom (the Supporting Information, Figure S14d), the adsorption energy is –1.01 eV. The most stable CAL adsorption configuration is the η^2 - π (C=C) adsorption (the Supporting Information, Figure S14e), with an adsorption energy of –1.02 eV. The most stable adsorption of the C=O bond on the Sn atom (the Supporting Information, Figure S14f) is –0.51 eV. The adsorption of C=C bond on Sn atoms is not feasible. From the result above, we can see that the activation of C=O did not preferentially occur on these two kinds of surfaces.

Finally, we considered the adsorption of CAL on the Pt₆/SnO_{2-x} surface with one O_{vac}. We compared the energy of slab with different O_{vac} and used the most stable O_{vac} as the computing model (Figure 6a and b). The adsorption of CAL by η²-di-σ(C=C) (Figure 6c) is slightly increased to -1.10 eV in the

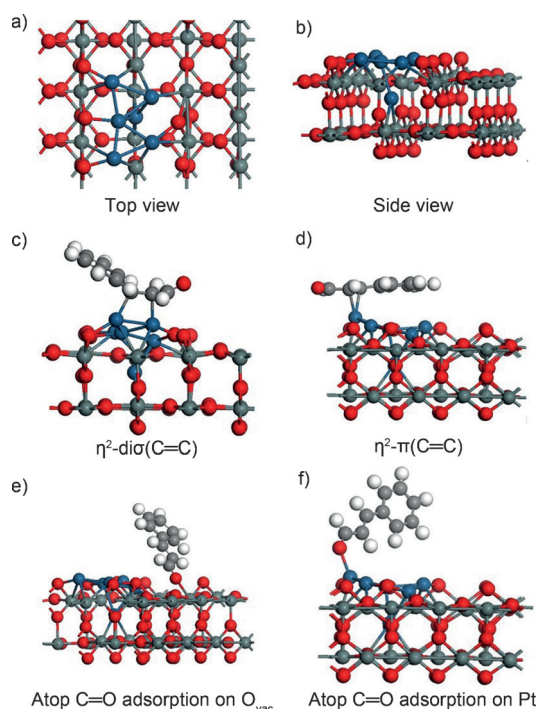


Figure 6. a, b) Catalyst model of Pt₆/SnO_{2-x} (110) surface with one O_{vac}; c–f) Adsorption configurations of CAL on Pt₆/SnO_{2-x} (110) surface with one O_{vac}. Blue, dark gray, red, gray, and white balls represent Pt, Sn, O, C, and H atoms, respectively.

presence of O_{vac} and the η²-π(C=C) adsorption (Figure 6d) is slightly increased to -1.05 eV. The adsorption energy by atop C=O adsorption on Pt (Figure 6f) is increased to -0.93 eV. The C=O adsorption is much stronger with the existence of O_{vac}. Moreover, the adsorption of C=O on the O_{vac} (Figure 6e) is stronger than the η²-di-σ(C=C) adsorption, with an adsorption energy of -1.13 eV. By comparing the adsorption energy of CAL on the Pt₆/SnO_{2-x} (110) with that of the Pt₆/SnO_{2-x} (110) surface containing one O_{vac}, we can see that the activation of C=O was considerably promoted on Sn atoms (from -0.51 to -1.13 eV) by taking the O_{vac} position. This may explain the increase of catalytic selectivity for C=O hydrogenation when the proportion of SnO increases and the selectivity to COL reached a plateau when the content of SnO was above 20% (Figure 5c). Although the η² adsorption energy of the olefin group was also as high as -1.10 and -1.05 eV in the presence of O_{vac}, the isolation of Pt atoms by Sn (the Supporting Information, Figure S4) may restrict this type of adsorption configuration.

Conclusion

We have found a composition-dependent structural evolution of monodispersed Pt–Sn NPs from SnO_{2-x}-patched PtSn alloy to a SnO_{2-x}-patched Pt cluster. Such unique structures secure the close contact between Pt and SnO_{2-x} and maximize the corresponding interface. In the hydrogenation of CAL, we have demonstrated that the O_{vac} sites, which are afforded by SnO_{2-x}, promote the adsorption of carbonyl group. The adsorbed species are subsequently hydrogenated by atomic hydrogen supplied by nearby Pt sites. Adjusting the proportions of the oxygen vacancy sites and the Pt sites leads to the optimum performance of 99% CAL conversion and 92% COL selectivity at ambient condition. This work represents a correlation between the bimetallic catalyst structure and the catalytic properties, and may pave a new avenue for advanced nanocatalysts in biomass conversion and electrocatalysis.

Experimental Section

Synthetic procedures of Pt NPs

Pt NPs were prepared following a similar procedure reported previously.^[23] In brief, [Pt(acac)₂] (19.6 mg) was dissolved in oleylamine (OAm) (6 mL) in a 25 mL two-neck round-bottom flask. The flask was heated to 100 °C in 20 min. Then a solution of OAm (1.5 mL) containing 80 mg of TBAB was injected into the flask and further heated to 120 °C, then kept at this temperature for 60 min.

Synthetic procedures of Pt–Sn NPs

Tetrabutylammonium borohydride (TBAB), OAm, and 1-octadecene (ODE) were used as the reductant, capping agent, and solvent, respectively. It should be noted that the timing of the addition of metal precursors and reductant is key to synthesize bimetallic Pt–Sn NPs: 1) [Pt(acac)₂] and [SnCl₂]₂H₂O cannot be added into the reaction flask until it has been heated to the designed temperature; 2) TBAB should be injected within one minute after the addition of metal precursors. Otherwise, the growth of Pt and Sn would undergo phase segregation as shown in Figure S9 (the Supporting Information). In a typical synthesis of Pt₅₀Sn₅₀, OAm (2 mL) and ODE (8 mL) were placed in a 25 mL two-neck round-bottom flask and heated to 130 °C to form a homogeneous solution. [SnCl₂]₂H₂O (11.2 mg) and [Pt(acac)₂] (19.6 mg) were added into the flask and the color of the reaction solution turned dark red. TBAB (100 mg) pre-dissolved in OAm (1 mL) was then injected into the flask immediately. The solution kept at 130 °C for 30 min. Following the same procedure, 3.8, 7.4, 16.9, 26.2 mg of [SnCl₂]₂H₂O and [Pt(acac)₂] (19.6 mg) led to the formation of Pt₇₅Sn₂₅, Pt₆₀Sn₄₀, Pt₄₀Sn₆₀, and Pt₃₀Sn₇₀ NPs, respectively.

XAS data analysis

The Pt–Pt scattering path with a coordination number of N=12 and bond length of R=2.81 Å in the face-centered cubic (fcc)-structured Pt bulk was used in the fitting of the Pt–Pt coordination. The Sn–O scattering path with a coordination number of N=6 and bond length of R=2.05 Å was used in the fitting of Pt–Sn NPs. The Pt–O scattering path with a coordination number of N=6 and bond length of R=1.98 Å was used in the fitting of Pt–Sn NPs. The Sn–Pt scattering path with a coordination number of N=6 and bond length of R=2.73 Å was used in the fitting of the

Pt₇₅Sn₂₅, Pt₆₀Sn₄₀, and Pt₅₀Sn₅₀ NPs. The Sn–Sn scattering path with a coordination number of N=2 and bond length of R=3.19 Å was used in the fitting of the Pt₅₀Sn₅₀, Pt₄₀Sn₆₀, and Pt₃₀Sn₇₀ NPs. The structural parameters, such as the coordination number N, the inter-atomic distance R, the Debye–Waller factor σ^2 , and the edge-energy shift ΔE_0 , were allowed to vary during the fitting process.

Computational details

All DFT calculations were performed using the CP2K program,^[24] which used a mixed Gaussian and plane wave (GPW) formalism for electronic structure calculations. The double- ζ valence plus polarization (DZVP) basis set and the Geodecker–Teter–Hutter (GTH) pseudopotential^[25] were used. The number of electrons considered in the valence shell for H, C, O, Sn, and Pt atoms were 1, 4, 6, 4, and 18, respectively. For the exchange–correlation potential, general gradient approximation (GGA) of Perdew–Burke–Ernzerhof^[26] (PBE) functional was used. An energy cutoff of 300 Ry was used for auxiliary PW expansion of the charge density. For geometry optimization calculations, the SCF convergence criteria is 10^{-6} a.u. and the maximum gradient was 4×10^{-4} a.u. For the calculations on SnO₂ (110) surface, a periodic slab model was used. The lattice constants of SnO₂ were also optimized. Because only the gamma point calculation is implemented in CP2K, the size of the super cell should be large enough to get a fine enough grid. For the optimization of the lattice constants, a $4 \times 4 \times 4$ super cell with initial size of $18.9491 \times 18.9491 \times 12.7455$ Å is used. The optimized lattice constants $a=b=4.842$ Å, $c=3.274$ Å, $u=0.3082$, are in good agreement with the previous calculation^[27] of SnO₂ using the CP2K program. For the calculation on the Pt (111) surface, a slab with a 6×6 surface and four atomic layers is used.

The adsorption energy is calculated according to Equation (1), in which $E_{\text{adsorbate}} + E_{\text{slab}}$ is the total energy of the adsorbate and the model slab, E_{slab} is the total energy of the model slab, $E_{\text{adsorbate}}$ is the total energy of the adsorbate in gas phase.

$$E_{\text{ads}} = E_{\text{adsorbate}} + E_{\text{slab}} - E_{\text{slab}} - E_{\text{adsorbate}} \quad (1)$$

Though the zero-point energy correction (ZPEC) may play a significant role in the adsorption energies, reaction energies, and reaction barriers, the relative adsorption energy difference of various configurations will not be significantly affected. In our calculations, no corrections of ZPEC are made.

Catalytic hydrogenation

Catalytic hydrogenation of cinnamaldehyde was performed in a single-neck flask. The solvent in NPs stock dispersion was removed under reduced pressure and the NPs (0.025 mmol Pt) were re-dispersed in *n*-butanol (3 mL) by sonication. The solution containing NPs, *n*-butanol, *n*-tetradecane (78 μ L, internal standard), and CAL (0.126 mL, 1 mmol) was then placed in a round-bottom flask, which was pre-purged with H₂. The reaction was then allowed to proceed at room temperature with a H₂ balloon under stirring (800 rpm). Samples were taken out at regular intervals, filtered, and analyzed by using GCMS. The selectivity to COL was measured at about 60% conversion of CAL, except that the selectivity for Pt₃₀Sn₇₀ is calculated on the conversion of 7%.

Acknowledgements

This research was supported by the State Key Project of Fundamental Research for Nanoscience and Nanotechnology (2011CB932401, 2011CBA00500, 2012CB224802), and the National Natural Science Foundation of China (21221062, 21131004, 21390393, U1463202).

Keywords: hydrogenation • nanoparticles • oxygen • platinum • tin

- [1] a) J. H. Sinfelt, *Acc. Chem. Res.* **1977**, *10*, 15–20; b) J. H. Sinfelt, J. L. Carter, D. J. C. Yates, *J. Catal.* **1972**, *24*, 283–296; c) J. H. Sinfelt, *J. Catal.* **1973**, *29*, 308–315; d) H. Rong, S. Cai, Z. Niu, Y. Li, *ACS Catal.* **2013**, *3*, 1560–1563.
- [2] a) C.-T. Wu, K. M. K. Yu, F. Liao, N. Young, P. Nellist, A. Dent, A. Kroner, S. C. E. Tsang, *Nat. Commun.* **2012**, *3*, 1050; b) C. Chen, Y. Kang, Z. Huo, Z. Zhu, W. Huang, H. L. Xin, J. D. Snyder, D. Li, J. A. Herron, M. Mavrikakis, M. Chi, K. L. More, Y. Li, N. M. Markovic, G. A. Somorjai, P. Yang, V. R. Stamenkovic, *Science* **2014**, *343*, 1339–1343; c) Q. Zhang, X. Guo, Z. Liang, J. Zeng, J. Yang, S. Liao, *Nano Res.* **2013**, *6*, 571–580; d) H. Wu, M. Xu, Y. Wang, G. Zheng, *Nano Res.* **2013**, *6*, 167–173.
- [3] a) M. Chen, D. Kumar, C.-W. Yi, D. W. Goodman, *Science* **2005**, *310*, 291–293; b) K.-Q. Sun, Y.-C. Hong, G.-R. Zhang, B.-Q. Xu, *ACS Catal.* **2011**, *1*, 1336–1346; c) R. Mu, Q. Fu, H. Xu, H. Zhang, Y. Huang, Z. Jiang, S. Zhang, D. Tan, X. Bao, *J. Am. Chem. Soc.* **2011**, *133*, 1978–1986; d) H. Wu, P. Wang, H. He, Y. Jin, *Nano Res.* **2012**, *5*, 135–144.
- [4] Y. Wu, S. Cai, D. Wang, W. He, Y. Li, *J. Am. Chem. Soc.* **2012**, *134*, 8975–8981.
- [5] S. C. Tsang, N. Cailuo, W. Oduro, A. T. S. Kong, L. Clifton, K. M. K. Yu, B. Thiebaud, J. Cookson, P. Bishop, *ACS Nano* **2008**, *2*, 2547–2553.
- [6] a) G. Chen, Y. Zhao, G. Fu, P. N. Duchesne, L. Gu, Y. Zheng, X. Weng, M. Chen, P. Zhang, C.-W. Pao, J.-F. Lee, N. Zheng, *Science* **2014**, *344*, 495–499; b) Q. Fu, W.-X. Li, Y. Yao, H. Liu, H.-Y. Su, D. Ma, X.-K. Gu, L. Chen, Z. Wang, H. Zhang, B. Wang, X. Bao, *Science* **2010**, *328*, 1141–1144.
- [7] a) K. B. Zhou, Y. D. Li, *Angew. Chem. Int. Ed.* **2012**, *51*, 602–613; *Angew. Chem.* **2012**, *124*, 622–635; b) S. Zafeiratos, S. Piccinin, D. Teschner, *Catal. Sci. Technol.* **2012**, *2*, 1787–1801; c) F. Tao, M. E. Grass, Y. W. Zhang, D. R. Butcher, F. Aksoy, S. Aloni, V. Altoe, S. Alayoglu, J. R. Renzas, C. K. Tsung, Z. W. Zhu, Z. Liu, M. Salmeron, G. A. Somorjai, *J. Am. Chem. Soc.* **2010**, *132*, 8697–8703; d) J. W. Hong, D. Kim, Y. W. Lee, M. Kim, S. W. Kang, S. W. Han, *Angew. Chem. Int. Ed.* **2011**, *50*, 8876–8880; *Angew. Chem.* **2011**, *123*, 9038–9042.
- [8] Q. Jia, W. Liang, M. K. Bates, P. Mani, W. Lee, S. Mukerjee, *ACS Nano* **2015**, *9*, 387–400.
- [9] S. Nishimura, *Handbook of heterogeneous catalytic hydrogenation for organic synthesis*, Wiley, New York, **2001**.
- [10] N. Ji, T. Zhang, M. Zheng, A. Wang, H. Wang, X. Wang, J. G. Chen, *Angew. Chem. Int. Ed.* **2008**, *47*, 8510–8513; *Angew. Chem.* **2008**, *120*, 8638–8641.
- [11] G. Ertl, H. Knözinger, F. Schüth, J. Weitkamp, *Handbook of Heterogeneous Catalysis, Vol. 8*, Wiley, **2008**.
- [12] a) T. Birchem, C. M. Pradier, Y. Berthier, G. Cordier, *J. Catal.* **1994**, *146*, 503–510; b) T. Birchem, C. M. Pradier, Y. Berthier, G. Cordier, *J. Catal.* **1996**, *161*, 68–77; c) C. M. Pradier, T. Birchem, Y. Berthier, G. Cordier, *Catal. Lett.* **1994**, *29*, 371–378.
- [13] M. Englisch, A. Jentys, J. A. Lercher, *J. Catal.* **1997**, *166*, 25–35.
- [14] M. A. Vannice, B. Sen, *J. Catal.* **1989**, *115*, 65–78.
- [15] P. Gallezot, D. Richard in *Catalysis Reviews, Vol. 40*, **1998**, pp. 81–126.
- [16] D. Richard, J. Ockelford, A. Giroir-Fendler, P. Gallezot, *Catal. Lett.* **1989**, *3*, 53–58.
- [17] Y. Uemura, Y. Inada, K. K. Bando, T. Sasaki, N. Kamiuchi, K. Eguchi, A. Yagishita, M. Nomura, M. Tada, Y. Iwasawa, *J. Phys. Chem. C* **2011**, *115*, 5823–5833.
- [18] J. P. Stassi, P. D. Zgolicz, S. R. de Miguel, O. A. Scelza, *J. Catal.* **2013**, *306*, 11–29.

- [19] P. Concepción, Y. Pérez, J. C. Hernández-Garrido, M. Fajardo, J. J. Calvino, A. Corma, *Phys. Chem. Chem. Phys.* **2013**, *15*, 12048–12055.
- [20] A. B. Merlo, B. F. Machado, V. Vetere, J. L. Faria, M. L. Casella, *Appl. Catal. A* **2010**, *383*, 43–49.
- [21] A. J. Plomp, D. M. P. van Asten, A. M. J. van der Eerden, P. Mäki-Arvela, D. Y. Murzin, K. P. de Jong, J. H. Bitter, *J. Catal.* **2009**, *263*, 146–154.
- [22] X. Yang, A. Wang, X. Wang, T. Zhang, K. Han, J. Li, *J. Phys. Chem. C* **2009**, *113*, 20918–20926.
- [23] V. Mazumder, S. Sun, *J. Am. Chem. Soc.* **2009**, *131*, 4588–4589.
- [24] J. VandeVondele, M. Krack, F. Mohamed, M. Parrinello, T. Chassaing, J. Hutter, *Comput. Phys. Commun.* **2005**, *167*, 103–128.
- [25] a) S. Goedecker, M. Teter, J. Hutter, *Phys. Rev. B* **1996**, *54*, 1703–1710; b) J. VandeVondele, J. Hutter, *J. Chem. Phys.* **2007**, *127*, 114105.
- [26] J. P. Perdew, K. Burke, M. Ernzerhof, *Phys. Rev. Lett.* **1996**, *77*, 3865–3868.
- [27] a) K. R. Hahn, A. Tricoli, G. Santarossa, A. Vargas, A. Baiker, *Surf. Sci.* **2011**, *605*, 1476–1482; b) G. Santarossa, K. Hahn, A. Baiker, *Langmuir* **2013**, *29*, 5487–5499.

Received: April 14, 2015

Published online on July 14, 2015